DOI: 10.1021/ma901428z

Macromolecules
ARTICLE

High Impact Properties of Polyketone/Polyamide-6 Alloys Induced by Characteristic Morphology and Water Absorption

Atsushi Asano,[†] Maiko Nishioka,[‡] Yohei Takahashi,[‡] Atsushi Kato,*[,‡] Shigeki Hikasa,[§] Hitoshi Iwabuki,[§] Kazuya Nagata,[∥] Hidenori Sato,[‡] Toshinori Hasegawa,[‡] Hisahiro Sawabe,[‡] Masazumi Arao,[‡] Toshiya Suda,[‡] Ayano Isoda,[‡] Mitsuo Mukai,[‡] Daisuke Ishikawa,[‡] and Toshihiro Izumi[‡]

[†]*Department of Applied Chemistry, National Defense Academy, Yokosuka 239-8686, Japan,* [‡]*NISSAN ARC, LTD., 1 Natsushima, Yokosuka 237-0061, Japan,* [§]*Industrial Technology Center of Okayama Prefecture, 5301, Haga, Okayama 701-1296, Japan, and* [∥]*Advanced Technology Development Department Laboratory of Plastics, Asahi Kasei Chemicals Corporation, 1-3-1, Yakou, Kawasaki 210-0863, Japan*

Received July 2, 2009; Revised Manuscript Received October 29, 2009

ABSTRACT: Nagata et al. recently developed high-impact polyketone/polyamide-6 (PK/PA) alloys and investigated their mechanical properties (Nagata et al. Polym. Prep. Jpn. **2006**, 55, 4286−4287). This paper presents the results of investigations of their morphology, such as the domain size of PA and PK, features of crystalline phase of PK (the long period and thickness of lamellae are deduced), and the change in crystalline form of PA in the PK/PA alloys, using solid-state nuclear magnetic resonance (NMR), small-angle X-ray scattering (SAXS), and transmission electron microscopy (TEM). Solid-state ^{13}C and ^{15}N NMR results revealed that the γ crystalline phase of PA changes into a thermodynamically stable α crystalline phase after alloying with PK. The difference in the long period of lamellae of PK/PA alloys between dry and wet conditions is discussed. We conclude that the characteristic morphology of PK and humidity of the amorphous phase of PA in the wet condition are very important factors enabling the PK/PA alloys to exhibit high impact resistance, high-strength, and high modulus.

Introduction

Polymer blends and alloys have been widely used for engineering purposes. The excellent physical/mechanical properties of polymer alloys, such as high impact resistance, high modulus, or strong toughness, are closely related to the highly controlled or ordered morphology and homogeneity of the raw materials used. However, the simple blending of polymers having good physical or chemical properties does not always produce materials possessing the desired qualities. Nonetheless, blending and alloying are the mainstream methods for developing engineering materials simply and reasonably. There are especially strong desires for the development of impact-resistant plastic materials that can be applied to auto parts to improve the safety of vehicles and increase fuel economy due to their lighter weight.

Recently, Nagata et al. have found that semicrystalline polyketone/polyamide-6 (PK/PA) alloys obtained in a simple blending process show better impact properties than would be expected from the simple addition of the impact energy of both PK and PA.[1] PK/PA alloys including over 30 mass % PA under a wet condition show an especially dramatic improvement in impact properties. The enhanced impact resistance is greater than that of polycarbonate (total impact value of approximately 10−90 $kJ \cdot m^{-2}$)[2] known as a high-impact engineering polymer. For the PK/PA alloys with over 30 mass % PA under a wet condition, the total impact value obtained in Charpy impact test (ISO 179-1:2000) was over 150 $kJ \cdot m^{-2}$ and close to 200 $kJ \cdot m^{-2}$ for some samples, whereas the value under a dry condition was less than 50 $kJ \cdot m^{-2}$ as shown in Figure 1. We have previously reported the relationship between impact property and water content based on Charpy impact test results, and that a weak interpolymer interaction between PK and PA surfaces was confirmed by the compositional dependence of Raman spectra.[3−5] Preliminary studies of the PK/PA alloys were also conducted by transmission electron microscopy (TEM) and small-angle X-ray scattering (SAXS). The TEM measurements revealed that the PK/PA alloys show a characteristic microstructure consisting of the PA-rich phase and a lamellar network of the PK-rich phase, which we call a cocontinuous nanolayer.

Our ultimate goal is to elucidate the detailed mechanism of the high impact properties of the PK/PA alloys under wet conditions and the overall relationship between their impact properties and morphology. In this study, however, our aim was to reveal how the morphology of the PK/PA alloys changes from that of pure PK and pure PA under both dry and wet conditions through the use of solid-state nuclear magnetic resonance spectroscopy (SSNMR), TEM, and SAXS measurements. We focused on investigation the relationship between morphology under a humid condition and impact properties.

Experimental Section

Materials. The polymer alloys examined consisted of semicrystalline polyketone (PK, an ethylene/propylene/CO copolymer $-(CH_2CH_2CO)_m-(CH_2CH(CH_3)CO)_n-$; Carilon D26H-M100, Shell Co.) and semicrystalline polyamide-6 (PA; $-(NH-(CH_2)_6CO)_k-$, Amilan CM1017, Toray Ind.). The sample indicated here as the K60A40 alloy means that it was blended of 60 mass % of PK (volume fraction 0.578) and 40 mass % of PA (volume fraction 0.422). The PK/PA alloys were moisture-conditioned by holding them at 50% or 95% relative humidity (RH) and a temperature of 23 °C for 3 weeks or more. Dry test specimens were prepared by drying them in a vacuum at 100 °C for 72 h. The moisture absorption rate was measured by the Karl

*Author for correspondence. E-mail kato@nissan-arc.co.jp.

 Published on Web 11/23/2009

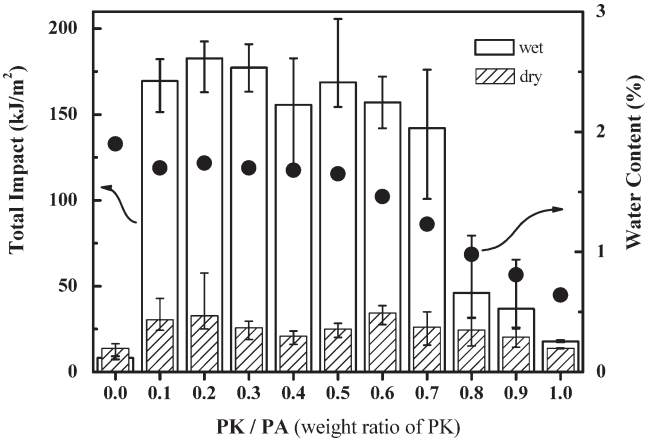

Figure 1. Total impact energy vs the weight ratio of PK for PK/PA alloys under dry and wet conditions. The water contents of wet samples obtained by the Karl Fisher method is also indicated by the solid circles.

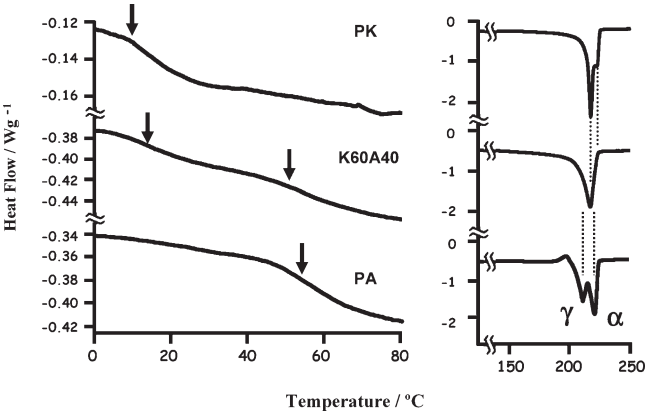

Figure 2. Observed DSC curves for pure PK, K60A40, and pure PA. The left-side graph is for the region from 0 to 80 °C and the right-side graph shows enlarged DSC curves for the melting endothermic peak region from 150 to 250 °C. The curves were obtained in the second scan.

Fisher method. The test specimens were then hermetically sealed in aluminum foil laminated bags and stored in a refrigerator until just prior to every measurement to avoid any change in the moisture condition.

Charpy Impact Test. Instrumented Charpy impact tests were conducted according to the procedure specified in JIS K 7111 (corresponding to ISO 179-1:2000) at a temperature of approximately 24 °C and at approximately 45% RH. The impact tester used was a CHARPAC-FRII (Yonekura MFG Co., Ltd.) and the data obtained were analyzed using IITMWin19 software (Yonekura MFG Co., Ltd.) designed for processing Charpy impact test data.

NMR. High-resolution solid-state ^{13}C nuclear magnetic resonance (^{13}C SSNMR) spectra were measured using a Varian NMR Systems 400WB spectrometer operating at 100.7 MHz for ^{13}C and 400.5 MHz for ^{1}H. The conventional cross-polarization (CP) and magic-angle spinning (MAS) with ^{1}H high-power dipolar decoupling technique was used, employing a rotor with a 4.0 mm diameter. The radio frequency field strength for ^{1}H decoupling was 120 kHz and the two-pulse-phase-modulation (TPPM) method[6] was used. The MAS frequency was 16 kHz and the ramped-amplitude CP method[7,8] was used. ^{13}C chemical shifts were measured relative to tetramethylsilane (TMS) using the benzene carbon signal at 132.07 ppm for solid hexamethylbenzene as an external standard. The ^{1}H spin−lattice relaxation times in the laboratory frame (T_1^H) were indirectly measured from well-resolved ^{13}C signals enhanced by a CP contact time of 2 ms applied after the inversion−recovery pulse sequence for the ^{1}H nucleus. The respective carbonyl carbon peaks were employed to obtain the T_1^H relaxation curves for PK and PA individually, because the peaks were measured separately. Therefore, the CP contact time is relatively long, but the maximum peak intensity was obtained at a CP contact time of 2 ms. ^{15}N SSNMR spectra were also measured with MAS = 5 kHz and a ^{1}H decoupling frequency of 65 kHz using a 7.5 mm diameter rotor. The CP contact time was 0.5 to 1 ms and was selected so as to obtain the maximum CP efficiency. ^{15}N chemical shifts were measured relative to the glycine signal as an external standard at 0 ppm. Every spectrum was measured at room temperature of ca. 24 °C.

TEM. Transmission electron microscope (TEM) images were collected using a HITACHI H-800 TEM with an accelerating voltage of 200 kV. Electron staining was done with a phosphotungstic acid solution. Three-dimensional TEM images were examined using a FEI Tecnai G2 F20 TEM with a tilting angle ranging from −70 to +70° for every 2° step. A mapping image of nitrogen atoms in the samples was obtained by electron energy loss spectroscopy (EELS) using the Tecnai G2 F20 TEM.

SAXS. Small-angle X-ray scattering (SAXS) investigations were carried out using a Bruker AXS Nano-STAR diffractometer. Data were collected with Cu Kα radiation (λ = 0.154 nm). The distance between the sample and the detector (camera length) was 106 cm.

DSC. Differential scanning calorimetry (DSC) was performed using a TA Instruments DSC-Q1000 at a temperature rise rate of 10 K·min^{-1} from 0 to 250 °C.

FT-IR. Variable-temperature Fourier-transform infrared (FT-IR) spectra were measured to determine the crystallization temperature, T_c, of both PK and PA in the alloys. The FT-IR spectra were examined with a Spectra-Tech IRμs system. Differential peak heights at 1695 cm^{-1} for PK and 1641 cm^{-1} for PA were observed during heating and cooling procedures at 10 K·min^{-1}.

Dynamic Mechanical Thermal Analysis (DMTA). DMTA was performed with a Seiko Instruments DMS-6100. Injection-molded specimens were subjected to bending (flexural) mode measurements at a scan rate of 2 K·min^{-1} and at a frequency of 10 Hz in a temperature range from −100 to +150 °C in a nitrogen gas atmosphere. In this analysis, the mechanical loss tangent delta (tan δ) was examined to find the T_g values of PK, PA, and the K60A40 alloy under both wet and dry conditions.

Results and Discussion

Charpy Impact Test. Figure 1 shows the Charpy impact test results for various PK/PA alloys under both dry and wet conditions. The Charpy impact test gives the total impact energy, which is related to impact resistance. The vertical axis of Figure 1 indicates total impact energy per unit cross-sectional area. A high energy value indicates the high impact resistance, high modulus, and high toughness of the material. In the dry condition, the total impact values of the PK/PA alloys are slightly higher than those of the PK and PA homopolymers for all of the compositions tested. It will be noted that the total impact values of the alloys under the wet condition show a surprisingly large increase, especially for the PK/PA alloys with a PA content of over 30 mass %. Interestingly, the wet pure PA sample does not show such an improvement, though it is seen even for the K10A90 alloy. The water content in the PK/PA alloys under the wet condition was proportional to the PA composition and became constant at a PA level of over 50 mass %. Figure 1 suggests that the impact properties are improved when the PA composition is over 30 mass % and the water content is over 1%. The improvement of impact strength under the wet condition is limited for the K80A20 and K90A10 alloys, and

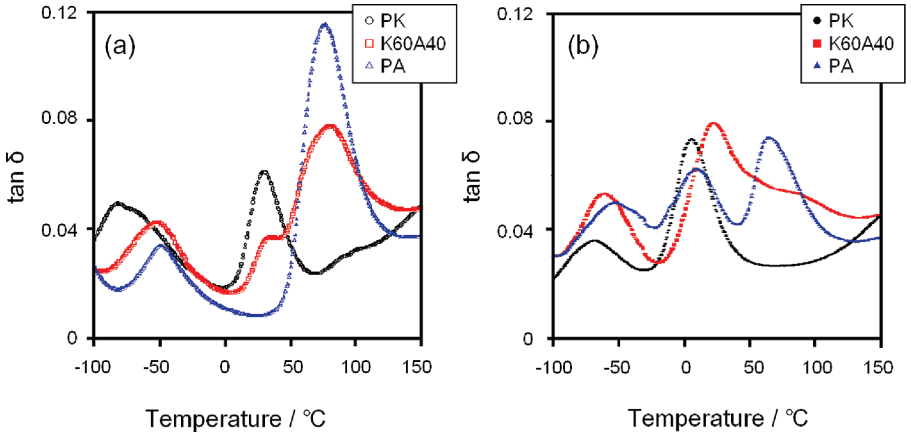

Figure 3. Loss tan δ vs temperature for pure PK, pure PA, and the K60A40 alloy under both (a) dry and (b) wet conditions. The frequency used was 10 Hz. The main dispersion corresponding to the glass transition (T_g) of pure PK is observed at ca. 30 °C and that of pure PA at ca. 78 °C for the dry condition. For the wet condition, the main dispersion of pure PK appears at ca. 5 °C and that of pure PA at ca. 65 °C. The subdispersions concerned in the impact property are also observed at lower temperature than T_g.

no improvement is seen for either pure PA or pure PK. Therefore, the pronounced improvement in impact resistance is presumably related to morphology and especially to the miscibility between PK and PA. This implies that it is valuable to investigate the relationship between morphology and humidity.

Miscibility and Morphology. First of all, we measured DSC curves to obtain information on miscibility and melting behavior in both crystalline phases of PK and PA in the PK/PA alloys. Figure 2 shows the DSC curves of pure PK, pure PA, and the K60A40 alloy under the dry condition. These curves were obtained in the second scan to avoid the effect of thermal history of samples as background. Other alloys examined showed similar DSC curves. The left-hand graph in Figure 2 represents the glass transition region and the right-hand graph the melting point (T_m) region. Usually, miscible and homogeneous blends or alloys show a single glass transition in the middle range of both distinct transitions.[9] However, the K60A40 alloy exhibits two different glass transitions, which are attributed to PK and PA, respectively, in the left-hand graph, although both glass transition temperatures (T_g's) become slightly closer. This indicates that the alloy is heterogeneous on a scale of several 10 nm,[9,10] but there are some interacting regions between PK and PA. The right-hand graph in Figure 2 shows that two endothermic transitions ascribed to the T_m of both the α and γ crystalline phases of pure PA are observed at 225 and 210 °C, respectively. The endothermic transition of pure PK is observed in the middle of these melting points of pure PA, and T_m is 220 °C. There is also another transition at a higher temperature as a shoulder peak for pure PK.

It is known that the endothermic transition of PK shows propylene unit dependence and doublet T_m peaks. PK has at least two kinds of crystallites, α (T_m = 245−250 °C) and β (T_m = 210−240 °C), and an increase in the propylene unit induces β crystallites from α crystallites.[11,12] Judging from the T_m value, the present crystalline phase is attributable to β crystallites. The reason for the small shoulder peak is unknown at present, but it may be related to the highly ordered crystalline phase of pure PK.

For the K60A40 alloy, a broad peak is observed at the middle point between those of the α and γ crystalline phases of pure PA and the T_m value is close to that of pure PK. The broad melting peak for the K60A40 alloy is shapeless and smooth. Therefore, the endothermic transition does not show any useful information about the morphology or change in crystalline phases of PA and PK.

In order to investigate the effect of humidity on T_g, we conducted a dynamic mechanical thermal analysis (DMTA) of pure PK, pure PA, and the K60A40 alloy under both dry and wet conditions. Figure 3 shows the observed DMTA curves (loss tan δ) in relation to temperature at a frequency of 10 Hz. The main dispersion corresponding to the glass transition is observed at approximately 30 °C for pure PK and that for pure PA at 78 °C under the dry condition (Figure 3a). The dispersion peaks for both pure PK and pure PA appear at different temperatures from the T_g values obtained by DSC. This shift usually occurs because the DMTA curves in Figure 3 show the change in the motional mode at a frequency of 10 Hz, whereas DSC measures the calorimetric change. These main dispersions are also observed for the K60A40 alloy at similar positions or with a slight shift toward an intermediate position. Each peak appears mostly at the same position but broadening occurs.

For the wet condition as shown in Figure 3b, the intensity of the loss tan δ curve of pure PA decreases compared with that of the dry condition, and a subdispersion at ca. 5 °C is newly observed. The main dispersion peaks for both pure PK and pure PA shift to 5 and 65 °C, respectively. These values are lower than those obtained under the dry condition. The loss tan δ curve of the K60A40 alloy under the wet condition shows a broad hump in the temperature region from 0 to 100 °C and the main dispersion peak is observed at ca. 23 °C.

Examination of the loss tan δ curves indicates that humidity influences the T_g values of every sample, causing the value to decrease. However, the impact strength values (total energy) obtained in the Charpy impact tests of both pure PK and pure PA do not show any effect of humidity at all, whereas the T_g values under the wet condition shift toward a lower temperature. This suggests that the effect of the decrease in T_g, which causes plasticization of PA or PK due to humidity, limits the improvement of impact strength. On the other hand, the subdispersions observed at a lower temperature than T_g presumably affect impact properties.[13] Therefore, it is also necessary to study the motional change of the local segment after alloying to elucidate the mechanism of the high impact properties of polymers as well as to reveal the morphology. In this study, we focused on to revealing the morphological change related to humidity in the PK/PA alloys in the first stage of this research because an

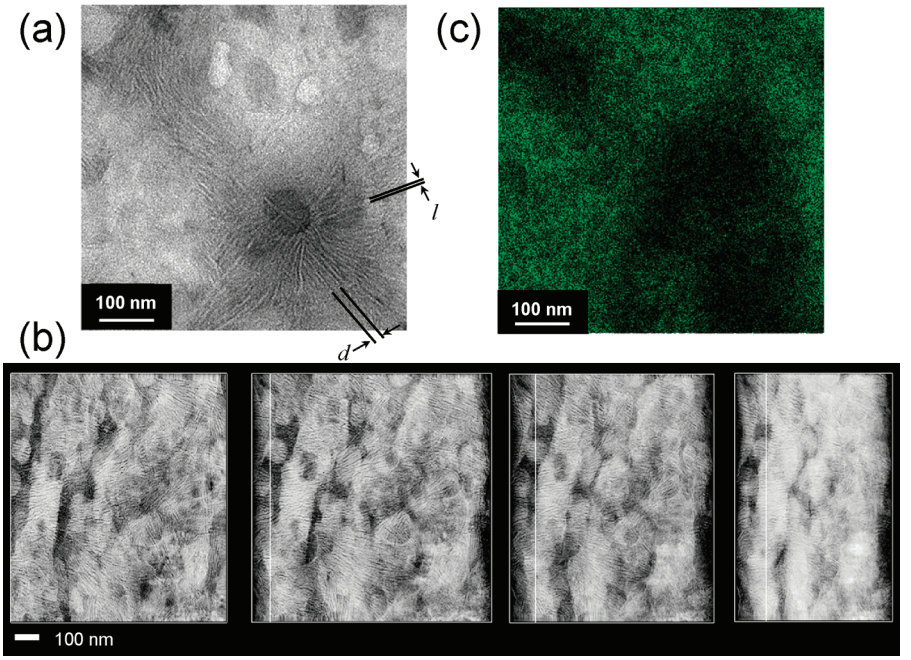

Figure 4. (a) TEM, (b) 3D-TEM, and (c) EELS images of K60A40. The 3D-TEM images in part b are views selected at arbitrary angles. The black and white contrast in the 3D-TEM images is the opposite of that in the TEM image. The long period of crystalline lamellae (distance between two lamellae), *d*, and the thickness of a lamellar rod, *l*, are indicated in the TEM image in part a. The green image of (c) represents nitrogen atoms mapping in the same region as that in part a.

overall morphological study is helpful in analyzing local segmental motion after alloying.

In order to study the morphology visually, we analyzed TEM, three-dimensional (3D)-TEM, and EELS images of the K60A40 alloy. Figure 4a shows a TEM image magnified 200000 times. Another TEM image of a different region is shown in Figure S1 in the Supporting Information. This TEM image indicates a lamellar-like structure resembling rods or thick lines and several elliptical domains of ca. 100 nm in size in the alloy. Since the amorphous phase is dominantly dyed, the black color represents mainly the amorphous region and the white color is the crystalline region. The lamellar-like structure is white in color, so it is the crystalline phase, namely crystalline lamellae. The black and white contrast around the lamellae indicates the repeated structure of the crystalline and amorphous phases. The lamellar thickness, *l*, (one rod) seems to be less than 5 nm and the long period (spacing, *d*, of two rods) of lamellae to be 10−20 nm. Lamellae are present both inside and outside the domains.

The 3D-TEM image (Figure 4b) gives a much clearer three-dimensional view of the presence of the PK lamellar-like structure inside the domains. To provide a clear view, the black and white contrast is alternated and indicates the opposite of that in the TEM image. Thus, the black color represents the crystalline phase and the white color the amorphous phase in Figure 4b. For both pure PK and pure PA, a lamellar-like structure was not clearly observed in the TEM image. However, a lamellar-like structure was detected even in the K90A10 alloy in the 3D-TEM image, albeit not clearly (Figure S2(c) in the Supporting Information).[4,5] This indicates that PA plays an important role in forming the lamellar-like structure. The results of a previous 3D-TEM study suggested that there are characteristic spherical domains on a scale of 50−200 nm in the PK-rich alloys, K90A10 or K80A20 (Figure S2 in the Supporting Information).[4,5] Figure 4b shows that there are cocontinuous spherical domains in the K60A40 alloy. These cocontinuous spherical domains of ca. 100 nm in size appear to be in the process of forming cylindrical domains. The results indicate that the complicated morphology observed for the PK/PA alloys stems from interactions between PK and PA. The occurrence of a weak interaction between PK and PA was revealed by analyzing the Raman spectra.[4,5]

To clarify which polymer forms the lamellar-like structure, we examined an electron energy loss spectroscopy (EELS) image of the K60A40 alloy. Figure 4c shows an EELS image that indicates the location of nitrogen atoms; the green color represents the nitrogen-rich region. The area shown in Figure 4c is the same region as in Figure 4a. By comparing the two figures, we can see that the area of the lamellar-like structure coincides with the location of PK chains. The black color represents the absence of nitrogen atoms, so PK chains contain no nitrogen. Even though the EELS measurement reveals the location of nitrogen atoms, there is some uncertainty as to whether the lamellae are formed by PK chains alone, because some green signals in Figure 4c coincide with the location of the lamellar area and are distributed widely; the black color is not in accord with the location of the lamellar-like structure completely and unambiguously. Furthermore, PA also forms both α and γ crystalline phases even in PK-rich alloys. The results of our previous 3D-TEM study also showed similar lamellar-like images even for PA-rich alloys, but the images were blurred (Figure S2(a) in the Supporting Information).[4,5]

The characteristic spherical and cylindrical structures as shown in Figure 4b are formed by the connection of both amorphous phases of PA and PK. The 3D-TEM images show that any numbers of PK lamellae are inserted in the cylindrical domains. After absorbing water, the K60A40 alloy shows excellent impact resistance. This implies that the cocontinuous structure with an elastic cylindrical PA-rich body and a rigid PK lamellar plane has a strong relation to the physical property of this PK/PA alloy under the wet condition. It is assumed that the rigid PK lamellae act like clay layers in polymer/clay nanocomposites.

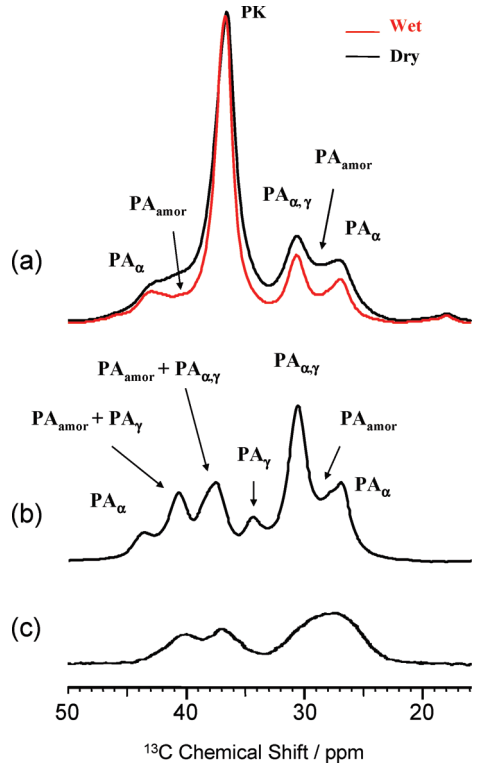

Figure 5. Observed and enlarged ^{13}C CPMAS SSNMR spectra for the aliphatic region of (a) K60A40 under dry and wet (red color) conditions. The spectrum in part b represents the ^{13}C SSNMR signals of pure PA before alloying under the wet condition. The spectrum in part c represents the amorphous phase of PA separated on the basis of the $T_{1\rho}^{H}$ difference.[14,15]

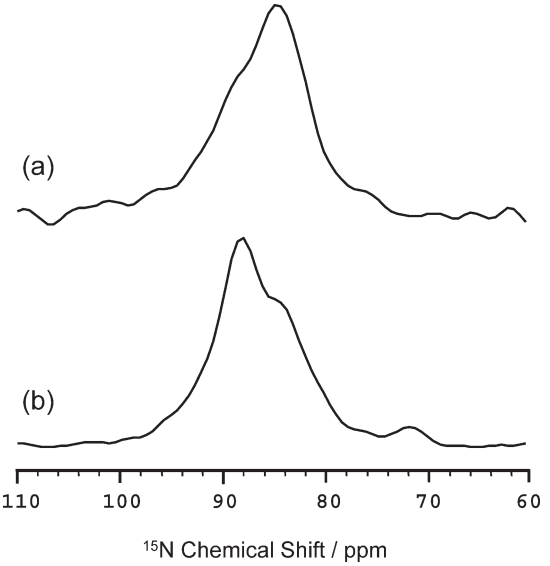

Figure 6. Observed ^{15}N CPMAS SSNMR spectra of (a) K60A40 and (b) pure PA. To show the peaks attributed to α and γ crystalline phases clearly, the spectra shown here were obtained from the sample under the wet condition. The reason is that the molecular motion of the water-absorbing amorphous polymer chain is fast, so its CP signal enhancement deteriorates and the overlapped amorphous signals can be eliminated effectively.

An investigation of the long period of the crystalline lamellae by SAXS measurements should yield useful information on the origin of the lamellar-like structure. Prior to discussing the lamellar interval and its origin quantitatively, we will discuss the crystalline phase structure of PA after alloying and the domains viewed in Figure 4 parts a and b.

Domain Size and Type of PA Crystalline Phase. Figure 5 shows the observed and enlarged solid-state ^{13}C CPMAS NMR spectra of the K60A40 alloy in the aliphatic carbon region. Figure 5a presents the ^{13}C CPMAS NMR spectra of the alloy for both dry and wet conditions. Figure 5b shows the ^{13}C CPMAS NMR spectrum of pure PA under the wet condition before alloying with PK. Figure 5(c) presents the ^{13}C CPMAS NMR spectrum of the amorphous signals of pure PA enhanced by using the difference in the ^{1}H spin−lattice relaxation time in the rotating frame ($T_{1\rho}^{H}$) between the crystalline and amorphous phases.[14,15] It is well-known that methylene carbons (CH_2) of PA reflect the environmental difference in the chain order of the crystalline phases, i.e., α and γ crystallites.[14−18] Therefore, the peaks of CH_2 resonated widely depending on its circumstance, and the assignment is depicted in the figure. Every CH_2 carbon of PK appears at 37 ppm as a single peak and the peak does not show any change before and after alloying. The methyl carbon of PK appears at 18 ppm as a very small peak.

Figure 5a shows that the ^{13}C CPMAS SSNMR signal intensity under the wet condition is lower than that under the dry condition. The relative intensity of the amorphous peak of PA decreases more markedly in the presence of moisture. This indicates that the CP efficiency of the amorphous phase declines. When water absorption occurs predominantly in the amorphous phase, the polymer chains display higher mobility than in the crystalline phase. Since CP works effectively between the ^{13}C and ^{1}H pair spins at a lower level of mobility, the CP efficiency between the mobile spins becomes worse.

The CH_2 signals of PK did not show any environmental dependence. Thus, the signals ascribed to both the crystalline and amorphous phases appear at the same chemical shift; the signal of the amorphous phase is probably broader than that of the crystalline phase. In Figure 5a, the line width of the peak at 37 ppm under the wet condition is somewhat narrower than that under the dry condition. However, the amorphous peak of PA also overlaps this area, so we can not conclude whether water absorption occurred in the amorphous region of PK as well as in that of PA. According to our earlier NMR observation (Figure S3 in the Supporting Information),[3−5] the carbonyl (C=O) peak of PK did not change after water absorption, while the C=O signal of PA decreased; each amorphous C=O peak was overlapped at the same respective chemical shift. Therefore, this observation indicates that water is absorbed predominantly in the amorphous phase of PA not that of PK.

Furthermore, the ^{13}C CPMAS SSNMR spectrum for PA of the K60A40 alloy (Figure 5a) appears to be simpler than that of pure PA (Figure 5b). This implies that the relative intensity of the signals ascribed to the γ crystalline phase of PA decreases. In order to clarify the difference in the crystalline phase of PA between pure PA and the alloy, we examined the ^{15}N CPMAS SSNMR spectra of both samples. Figure 6 shows the ^{15}N CPMAS SSNMR spectra of (a) the K60A40 alloy and (b) pure PA under the wet condition. It is well-known that the ^{15}N SSNMR signal is sensitive to the difference in the polymer chain direction between the α and γ crystalline phases of PA and shows a different chemical shift, which is due to the difference in the circumstances of hydrogen bonding.[18−20] The signal ascribed to the α crystalline phase of PA resonates at 84 ppm and that to the γ crystalline phase at 89 ppm.[19] Obviously, the α crystalline phase of PA in the K60A40 alloy (Figure 6a) is dominant compared with that of pure PA (Figure 6b): rapid cooling of PA induced the growth of the γ crystalline phase in pure PA.

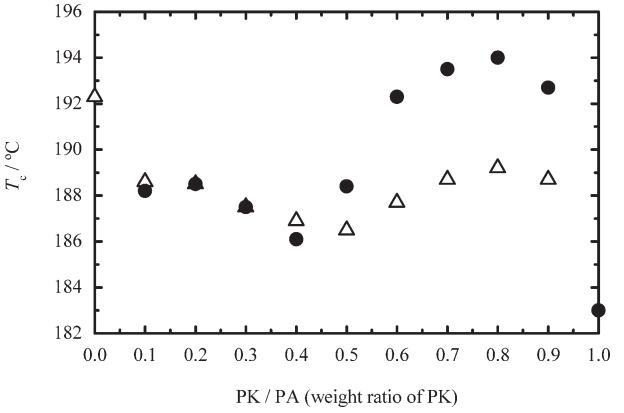

Figure 7. Compositional dependence of crystallization temperatures, T_c, of PK and PA for PK/PA alloys. Solid circles represent T_c of PK and open triangles that of PA. The temperatures were determined by analyzing the IR signal change during the cooling stage from the melting state of crystalline phase (Figure S5 in the Supporting Information).

This indicates that PK induces the growth of the α crystalline phase of PA in the alloy rather than γ crystallites. This observation is consistent with the results of the ^{13}C CPMAS SSNMR experiment. The relative fraction of the α crystalline phase of PA, which is obtained from spectral deconvolution by two pseudo-Voigt functions, changes from 40% to 70% after alloying with PK. A pseudo-Voigt function is expressed as the sum of the Gaussian and Lorentizan curve functions (Figure S4 in the Supporting Information).

In the case of blending with clay minerals, in contrast, the relative fraction of the α crystalline phase of PA usually decreases and the amount of the γ crystalline phase increases independent of the cooling history.[15,21] This suggests that PK induces the thermally stable α-crystalline phase of PA in the alloy and that the lamellar-like structure of PK is stabilized by the alternating of the crystalline phase of PA between parallel (γ) and antiparallel (α) chain directions. Presumably, PK causes the crystallization temperature of PA to decrease, because a higher crystallization temperature induces γ crystallites and there are no orientated materials to create γ crystallites. The change in the crystalline form of PA is related to the complicate morphology detected in the TEM image and to the high impact properties under the wet condition.

That PK stabilizes the α-crystalline phase of PA is supported by the crystallization temperature as shown in Figure 7. In order to detect each crystallization temperature, T_c, we measured FT-IR spectra during the heating and cooling stages, because the DSC curves during the cooling stage did not show any distinct exothermic transitions attributable to crystallization of PK and PA. The T_c of PK was detected by increasing the ratio of the IR peak at 1695 cm^{-1} attributed to vibration of the C=O functional group. Similarly, the increase in the IR peak at 1641 cm^{-1} attributable to NHCO vibration was used for detecting the T_c of PA (Figure S5 in the Supporting Information).

Figure 7 shows that the T_c of PK increases rapidly with a small amount of PA, while the T_c of PA decreases as a result of alloying with PK. The T_c of PA in the PK/PA alloy becomes relatively constant at 188 ± 1 °C, down from 192 °C for pure PA. The T_c of PK in the PK-rich/PA alloy is 191 ± 1 °C and that in the PK/PA-rich alloy is 188 ± 1 °C, up from 183 °C for pure PA. It is interesting that the PK-rich/PA alloy shows a much larger increase in T_c than the PK/PA-rich alloy. This suggests that a small amount of PA strongly affects the crystalline growth of PK, and this is in agreement

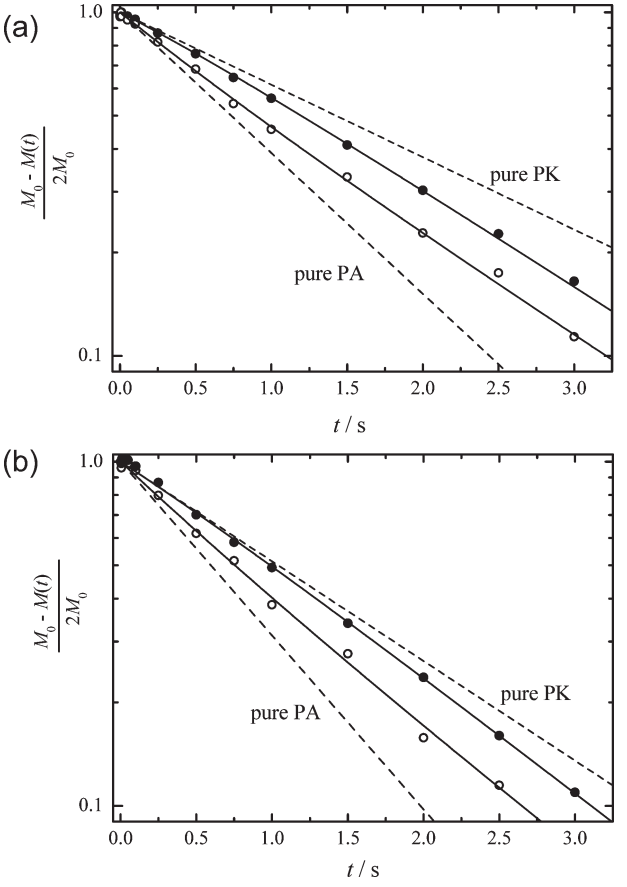

Figure 8. Semilogarithmic plots of normalized T_1^H decay curves for PK (●) and PA (○) in the K60A40 alloy under the (a) dry and (b) wet conditions. Dashed lines represent T_1^H decay curves for pure PA and pure PK. The solid lines were obtained with eq 1.

with our previous 3D-TEM study in which lamellae were observed even in the K90A10 alloy (Figure S2 in the Supporting Information).[4,5] Thus, the data in Figure 7 obviously suggest that the T_c of PK increases by alloying with PA but that the T_c of PA decreases by alloying with PK. The former increase indicates that PK easily forms a crystalline phase with PA. In the case of PA/clay nanocomposites, the T_c of PA is higher than that of pure PA.[15] This is because PA chains can align along the clay surface first and form γ crystallites easily. In contrast, much more time and a lower temperature are needed to create α crystallites. Figure 7 shows the contrastive results for PA/clay nanocomposites. The lower T_c suggests that PA predominantly forms α crystallites in PK/PA alloys. This is in good agreement with the ^{13}C and ^{15}N SSNMR results.

Figure 8 shows the observed ^1H spin−lattice relaxation curves in the laboratory frame (T_1^H curves) of both PK and PA in the K60A40 alloy. These T_1^H curves were obtained from the C=O carbon peaks of PK and PA, respectively. Because both C=O carbons are close to the protons of the main chain aliphatic carbons or NH (see the chemical formula in Figure S3 in the Supporting Information), ^1H spin diffusion occurs efficiently even though protons are not bonded directly to carbon within the CP contact time of 2 ms. The T_1^H curves shown in Figure 8a are for the dry condition and those in Figure 8b are for the wet condition. The T_1^H curves of both pure PK and pure PA (dashed lines) show single exponential decay, resulting in semilog plots in a straight line. The T_1^H values for pure PK and pure PA under the dry condition are 2.06 ± 0.03 s ($1/T_1^H = K = 0.485\ s^{-1}$)

and 1.06 ± 0.01 s (K = 0.943 s^{-1}), respectively: errors are standard deviation. The values under the wet condition are 1.50 ± 0.01 s (K = 0.667 s^{-1}) for PK and 0.86 ± 0.01 s (K = 1.163 s^{-1}) for PA. The T_1^H rates, K, under the wet condition are faster than those under the dry condition. This indicates that the molecular motion of both polymers is affected and is increased by water absorption. For PA, water is absorbed predominantly in the amorphous phase and the humidity is 1.9%; for the PA-rich alloys, the humidity is 1.7%. On the other hand, PK absorbs water without selectiveness and the amount of absorbed water is only 0.6%. This difference in water absorption shows that the ^{13}C CPMAS NMR spectrum of PK remains unchanged under the wet condition, but that there is sufficient water absorption to change the molecular motion and affect the T_1^H of PK. In fact, Figure 3 shows a decrease in the T_g of PK under the wet condition, indicating that the molecular motion was faster at the measured temperature of about 24 °C.

The T_1^H decays of both polymers in the alloy draw closer together. In the case of miscible blends on a scale of several tens of nanometers, the observed T_1^H decays show a single exponential curve and have identical values owing to the very fast ^1H spin-diffusion phenomenon in the solid state between component polymers.[10,22] In the case of heterogeneous blends, on the other hand, the observed T_1^H decays in a blend do not change and show the same relaxation curves as those of the pure materials. Therefore, the results in Figure 8 suggest that both PK and PA are not completely phase-separated but are located in an area where both polymers can interact via ^1H spin diffusion (Figure S6 in the Supporting Information). Provided that the domains of the blends or alloys have an adequate size less than approximately 200 nm: this value depends on $1/T_1^H$ rate,[23,24] the observed T_1^H curves of such a two-spin system exhibit nonsimple and nonusual double-exponential decays as follows:[25]

$$M_{PK}(t) = a_+ \exp(r_+ t) + a_- \exp(r_- t)$$

$$M_{PA}(t) = b_+ \exp(r_+ t) + b_- \exp(r_- t) \quad (1)$$

where

$$a_\pm = 1 \pm R^{-1}(K_{PA} - K_{PK} + k),$$
$$b_\pm = 1 \pm R^{-1}(K_{PK} - K_{PA} + k)$$

$$r_\pm = 0.5\{-(K_{PK} + K_{PA} + k) \pm R\},$$
$$R = \sqrt{\{(K_{PK} - K_{PA}) + (f_{PA} - f_{PK})k\}^2 + 4f_{PA}f_{PK}k^2}$$

Here, $M_i(t)$, f_i, K_i, and k denote the normalized magnetization, proton molar fraction, the intrinsic relaxation rate of i-spin: i is for PK and PA, and the ^1H spin-diffusion rate between PK and PA proton spins, respectively. The sum of f_{PK} and f_{PA} equals 1.

In the case of semicrystalline polymers, the amorphous phase is usually located in the vicinity of the crystalline phase and very fast ^1H spin diffusion occurs between the two phases.[26] Therefore, PK/PA alloys can be divided into two spin species of PK spin and PA spin; the individual crystalline phase has the same spin temperature as that of the amorphous phase. The purpose of this analysis is to determine the spatially averaged domain size of the spins for PK and PA in the alloy under both dry and wet conditions. A T_1^H analysis provides information on the averaged domain size of both PK and PA; TEM, on the contrary, does not provide information on the respective domain size. A TEM image only shows the black and white contrast and we do not know which color represents which polymer. Estimation of domain size is helpful in analyze the morphology based on TEM images.

The solid lines in parts a and b of Figure 8 were obtained from a least-squares fitting using eq 1 with f_{PA} of 0.548. The solid lines are in excellent agreement with the observed T_1^H decay curves (● and ○) in the K60A40 alloy. The K values obtained for the dry condition are 0.53 ± 0.02 s^{-1} (1.90 s) for PK and 0.81 ± 0.02 s^{-1} (1.21 s) for PA, respectively: the values in parentheses are $1/K = T_1^H$. The ^1H spin-diffusion rate, k, is 0.8 ± 0.3 s^{-1}. The values obtained for the wet condition are K_{PK} = 0.66 ± 0.04 s^{-1} (1.51 s), K_{PA} = 0.95 ± 0.04 s^{-1} (1.05 s), k = 0.7 ± 0.5 s^{-1}, respectively.

The initial relaxation rate of PA, K_{PA}, in the alloy is more affected by alloying with PK than that of PK. The K_{PA} value is slower than that of pure PA by ca. 0.2 s^{-1}, whereas that of PK in the alloy is comparable to that of pure PK. This observation suggests that PA dispersed and located in PK matrix, rather than that both PA and PK are alternatively aligned. It also indicates that the molecular motion of PA is greatly affected after alloying with PK. The images in Figure 4 suggest that the lamellae are also present in the cocontinuous spherical and cylindrical domains (see also Figures S1 and S2 in the Supporting Information). The EELS observation reveals that the lamellae are mainly created by PK chains. Therefore, since the molecular motion of the rigid PK lamellar structure is not influenced by PA, the initial relaxation rate does not change after alloying, whereas that of PA is altered. On the other hand, the spin-diffusion rate, k, is comparable to the initial relaxation rate of both polymers and intermediate between K_{PK} and K_{PA}. This value indicates that ^1H spin diffusion is slow, but that the two polymers are not completely phase-separated on a scale of several tens to several hundreds of nm.

The maximum diffusive path length, $\langle r^2 \rangle^{0.5}$ (i.e., average value of r), for the three-dimensional diffusion model is estimated by $(6D/k)^{0.5}$; D is the diffusion coefficient for proton spin energy. In the case of semicrystalline polymers, it may be better to assume the one-dimensional model to determine the domain size and the thickness of crystalline phase. However, since the TEM images show that the direction of the lamellae is not uniform, the diffusion of proton spin energy results in every direction, i.e., the three-dimension. The effective D value[27−29] has been estimated to be ca. 700 nm^2 s^{-1} from both diffusion coefficients D_{PK} = 840 nm^2 s^{-1} and D_{PA} = 600 nm^2 s^{-1}, which were obtained from the ^1H spin−spin relaxation rate.[30] The estimated path length, r, is ca. 77 nm, thus the average domain size is ca. 150 nm, which is twice as large as r. This value is consistent with the averaged overall size of the elliptical (or spherical and cylindrical) domains measured from the TEM images (Figure 4). Since the individual domains of PA and PK are not detected in the TEM images, the T_1^H measurement is useful in investigating the domain size of component materials, although this estimation is not exact.

We have also analyzed $T_{1\rho}^H$ for both polymers, though the data are not shown here.[30] Each observed $T_{1\rho}^H$ decay curve for PK and PA in the alloys agreed with those of the pure materials, respectively. This is not surprising, because $T_{1\rho}^H$ decay is sensitive to a much smaller domain size than 20 nm,[10,22] in other words, each $T_{1\rho}^H$ decay in the alloy is not influenced by such a slow ^1H spin diffusion rate of 0.7 s^{-1}.

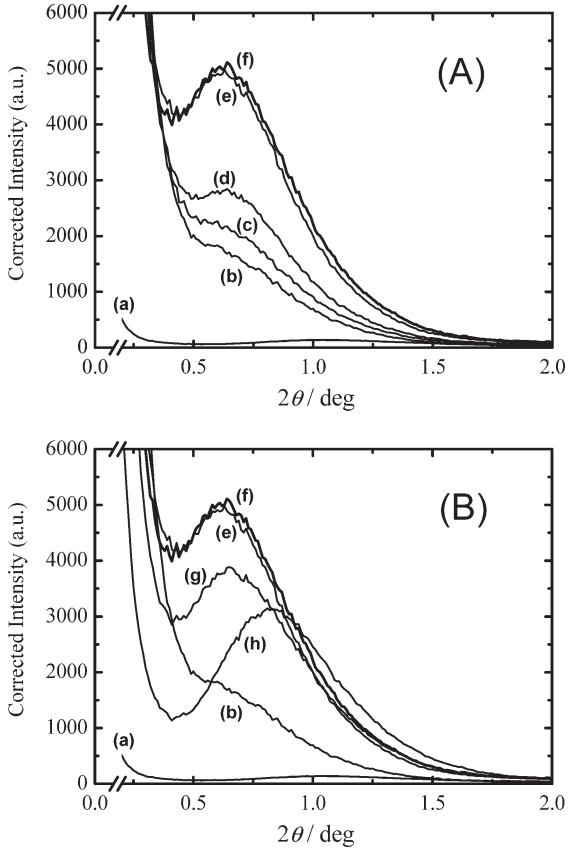

Figure 9. Observed and enlarged SAXS intensity profiles of PK/PA alloys, pure PK, and pure PA under the wet condition. Graph A presents SAXS intensity profiles from K90A10 to K60A40 and graph B those from K70A30 to K20A80: (a) pure PA, (b) pure PK, (c) K90A10, (d) K80A20, (e) K70A30, (f) K60A40 (bold line), (g) K50A50, and (h) K20A80. The intensity was normalized to the X-ray transmittance of the respective sample.

Long Period of PK Crystalline Phase. In order to investigate the long period of crystalline lamellae, we examined the SAXS intensity profile of every sample. Figure 9 shows the SAXS intensity profiles of pure PK, pure PA, and some PK/PA alloys under the wet condition. These intensity profiles were obtained as the integral of the SAXS scattering pattern on the horizontal axis. Hence, this observation reveals the amount and direction of lamellae in the PK/PA alloys. The SAXS intensity profiles were also examined under the dry condition to investigate the effect of water absorption on SAXS profile.

A broad peak is observed weakly at $2\theta = 0.62°$ for pure PK (b). The peak at $2\theta = 0.62°$ intensifies with an increase in PA content from K90A10 (c) to K60A40 (f). For the K60A40 (f) or K70A30 (e) alloys, an intense single peak is clearly observed at this angle. This increase corresponds to the results of the Charpy total impact measurements shown in Figure 1; the Charpy total impact energy values are low for K90A10 and K80A20, while the values of K70A30 and K60A40 are markedly larger. The peak at $2\theta = 0.62°$ indicates the formation of ordered lamellae of PK observed in TEM images in Figures 4a and 4b (Figures S1 and S2 in the Supporting Information). This implies that the increase in both the amount and ordered structure of the crystalline phase of PK is involved in the larger Charpy total impact energy, i.e., the higher impact resistance. Based on Bragg's law, the long period of these lamellae can be estimated to be 14.3 nm. This value is in accord with the *d* value estimated from the TEM images.

For PA content over 50 mass %, namely for the alloys from K50A50 to K10A90, the peak shifts toward a wider angle as shown in Figure 9B; only the SAXS profiles of K50A50 and K20A80 are shown. The peak of K20A80 is observed at 2θ = ca. 0.80°. This value is close to that of pure PA, the SAXS peak of which is observed at 2θ = ca. 1.05° as a very weak hump.[31] Furthermore, the peak intensity of the PA-rich alloys decreases with increasing PA content. Since the impact resistance is still high even for the PA-rich alloys (Figure 1), these observations are contradictory to the foregoing discussion that the peak at $2\theta = 0.62°$ appears to be related to the Charpy total impact energy values. The estimated long period of the lamellae of pure PA is 8.4 nm and that of K20A80 is 11.0 nm. The long period estimated for K20A80 is in-between that of the PK-rich alloys and pure PA, and the intensity is noticeably stronger than that of pure PA. Therefore, the SAXS peak at $2\theta = 0.80°$ for K20A80 presumably represents the presence of the lamellae of both PK and PA; that is, the long period of crystalline lamellae of PA becomes uniform and its direction is ordered by the surrounding ordered crystalline lamellae of PK with an increase in PA content. The SAXS profile thus becomes a composite peak consisting of the sum of the peaks of both PK and PA lamellae. This observation suggests that the total impact toughness of the PA-rich alloys may be due to a different mechanism from that of the PK-rich alloys. In fact, the energy of crack propagation (E_2) of the PA-rich alloys is larger than that of the PK-rich alloys, while the energy of crack generation (E_1) of the PA-rich alloys is smaller than or comparable to that of the PK-rich alloys: the sum of E_1 and E_2 is the Charpy total impact energy.[4]

Similarly, the SAXS intensity profiles under the dry condition were also examined. Each profile was similar in intensity, but the angle of peak intensity shifted slightly toward a wider angle by 0.04°.[31] For example, the peak intensity of the K60A40 alloy was observed at $2\theta = 0.66°$. This means that the long period of the crystalline lamellae was shortened by ca. 1 nm. This observation indicates that the amorphous phase swells in the wet condition and then the long period becomes wider. Thus, the amorphous phases of both PA and PK are located in-between the crystalline lamellae of PK, because water is absorbed in the amorphous phase of PA selectively as was revealed by the ^{13}C CPMAS SSNMR spectra (Figures 5 and S3 in the Supporting Information). This coexistence produces the smooth ^1H spin diffusion between PK and PA, and both T_1^H curves are influenced effectively.

The results of the ^1H spin−lattice relaxation experiments did not reveal any difference in domain size between the dry and wet conditions; i.e., the ^1H spin-diffusion rates were the same (Figure 8). Since the domain size of the amorphous phase increased just 1 nm under the wet condition, the T_1^H relaxation experiments were not influenced by such a small change. Thus, the T_1^H relaxation experimental results in Figure 8 are convincing. Of course, the amorphous phase exists not only between lamellae, but also the white contrast body seen in the 3D-TEM image in Figure 4b was created by the amorphous phases of both PK and PA. Therefore, the results in Figure 9 do not show any intrinsic swelling in size of the PA amorphous phase due to water. However, it is noteworthy that water content of only 1.5% is related to the dramatic improvement in impact resistance (Figure 1). Although the detail mechanism of high impact resistance involves a lot of the other factors, as well as the fracture mechanics theory, the present study suggests that the swelling of the amorphous phase of PA due to water absorption contributes to imparting elasticity and the characteristic

crystalline lamellae of PK are conducive to producing stiffness together with a complex morphology.

Conclusions

The results of this study show that the PK/PA alloys examined have complex morphology consisted of crystalline lamellae and spherical and cylindrical domains. PK lamellae are present in both domains and ordered PA lamellae are also found in the PA-rich alloys. ^{1}H spin diffusion analysis provides each averaged domain size of PK and PA, which is roughly estimated to be 150 nm. The ^{15}N SSNMR results revealed that the mixed PA crystalline phases of α and γ crystallites changes mainly to a thermally stabilized α crystalline phase after alloying with PK, thus the PA structure is influenced by the presence of PK. Similarly, PK chains are also affected by the presence of PA. PK crystalline lamellae are evidently formed only by alloying with PA as revealed by TEM. The ^{13}C SSNMR results indicated that water is only absorbed in the amorphous phase of PA in the alloys. A SAXS study suggested that the long period of PK lamellae is 13−14 nm, and the value increases by 1 nm after water absorption. This is indirect evidence of the presence of both PA and PK amorphous phases in-between lamellae of PK, because the amorphous phase of PK does not absorb water appreciably. Therefore, the PK crystalline lamellae, with a thickness is ca. 5 nm as found by TEM, and the water-absorbing amorphous phase of PA play an important role in enabling PK/PA alloys to exhibit high impact properties and toughness. This role resembles the function of the good dispersion of clay layers in polymer/clay nanocomposites in displaying high modulus, toughness, and other properties. The PK lamellae exhibit rigidity and stiffness, and water-absorbing amorphous phase of PA shows elasticity and softness. This combination of characteristics is needed to obtain high impact properties, modulus, and toughness. It should be pointed out that the change in crystalline type from γ-crystallites to α-crystallites is also important for high impact properties, and it probably helps create the PK lamellae efficiently.

Finally, we must note that the mechanism of impact resistance in polymer alloys[32] includes the formation of crazes or cavitations,[32−34] shear (yield) deformation[32,35] and absorption of impact energy by the fracturing of the adhesive interface[36] between the matrix and the dispersion phase. Since we concentrated on an investigation of morphology in this study, a discussion of the mechanism producing high impact properties under the wet condition is still lacking. We have already examined TEM images of fractured PK/PA alloys under both dry and wet conditions, but the other examinations are currently under way. In our next study, we plan to elucidate the mechanism of the high impact properties of PK/PA alloys under the wet condition using the fracture mechanics theory combined with the present morphological results and the other mechanical data.

Acknowledgment. We want to thank Mr. Junzou Ootake, technical adviser at the Industrial Technology Center of Okayama Prefecture, for his helpful discussions and technical advice. We also thank Mr. Masaru Hashimoto, Mr. Tadashi Awatani, Dr. Olga Drozdova, Ms. Ritsuko Kitano, and Mr. Takeo Okamura at NISSAN ARC for their valuable cooperation with this study.

Supporting Information Available: Figures showing a TEM image of K60A40 alloy, 3D TEM images at arbitrary angles, solid-state ^{13}C CPMAS NMR spectra ^{15}N CPMAS NMR spectra, FT-IR spectra of C=O regions of both PK and PA, and enlarged semi-logarithmic plots of normalized T_1^H decay curves. This material is available free of charge via the Internet at http://pubs.acs.org.

References and Notes

(1) Nagata, K.; Hikasa, S.; Hirotani, M.; Nitto, Y.; Watanabe, T. *Polym. Prep. Jpn*., **2006**, *55*, 4286−4287.
(2) For example, see web sites: http://www.engineeringpolymers.com/epbb/ch07.html or http://www.matweb.com/Search/MaterialGroupSearch.aspx?GroupID=26
(3) Asano, A.; Nishioka, M.; Kato, A.; Takahashi, Y.; Sawabe, H.; Arao, M.; Sato, S.; Sato, H.; Izumi, T.; Drozdova, O.; Ishikawa, D.; Hasegawa, T.; Okamura, T.; Nagata, K.; Hikasa, S.; Iwabuki, H. *Polym. Prepr*. **2008**, *49*, 682–683.
(4) Kato, A.; Nishioka, M.; Takahashi, Y.; Suda, T.; Sawabe, H.; Isoda, A.; Drozdova, O.; Izumi, T.; Nagata, K.; Hikasa, S.; Iwabuki, H. Asano, A. *J. Appl. Polym. Sci*., in press.
(5) Kato, A.; Nishioka, M.; Takahashi, Y.; Hikasa, S.; Iwabuki, H.; Nagata, K.; Asano, A. *Nippon Gomu Kyokaishi* (*J. Soc. Rubber Ind., Jpn*.), **2009**, *82*, 167−174 (in Japanese).
(6) Bennet, A. E.; Rienstra, C. M.; Auger, M.; Lakshmi, K. V.; Griffin, R. G. *J. Chem. Phys*. **1995**, *103*, 6951–6958.
(7) Peersen, O. B.; Wu, X.; Kustanovich, I.; Smith, S. O. *J. Magn. Reson*. **1993**, *A104*, 334–339.
(8) Metz, G.; Wu, X.; Smith, S. O. *J. Magn. Reson*. **1994**, *A110*, 219–227.
(9) Utracki, L. A. *Polymer Alloys and Blends—Thermodynamics and Rheology*; Carl Hanser-Verlag: Münich, Germany, 1989.
(10) Asano, A.; Takegoshi, K. In *Solid State NMR of Polymers*; Ando, I., Asakura, T., Eds.; Elsevier Science B.V.: Amsterdam, The Netherlands, 1998; Chapter 10, pp 351−414.
(11) Lagaron, J. M.; Vickers, M. E.; Powell, A. K.; Davidson, N. S. *Polymer* **2000**, *41*, 3011–3017.
(12) Lagaron, J. M.; Vickers, M. E.; Powell, A. K.; Bonner, J. G. *Polymer* **2002**, *43*, 1877–1886.
(13) Matsuoka, S. *Relaxation phenomena in polymers*; Carl Hanser-Verlag: Münich, Germany, 1992.
(14) VanderHart, D. L.; Asano, A.; Gilman, J. W. *Macromolecules* **2001**, *34*, 3819–3822.
(15) VanderHart, D. L.; Asano, A.; Gilman, J. W. *Chem. Mater*. **2001**, *13*, 3781–3795.
(16) Weeding, T. L.; Veeman, W. S.; Gaur, H. A.; Huysmans, G. B. *Macromolecules* **1988**, *21*, 2028–2032.
(17) Okada, A.; Kawasumi, M.; Tajima, I.; Kurauchi, T.; Kamigaito, O. *J. Appl. Polym. Sci*. **1989**, *37*, 1363–1371.
(18) Hatfield, G. R.; Glans, J. H.; Hammond, W. B. *Macromolecules* **1990**, *23*, 1654–1658.
(19) Mathias, L. J.; Davis, R. D.; Jarrett, W. L. *Macromolecules* **1999**, *32*, 7958–7960.
(20) Andreis, M.; Koenig, J. L. *Adv. Polym. Sci*. **1995**, *124*, 191–237.
(21) VanderHart, D. L.; Asano, A.; Gilman, J. W. *Chem. Mater*. **2001**, *13*, 3796–3809.
(22) Asano, A. In *Modern Magnetic Resonance*; Webb, G. A., Ed.; Springer: Dordrecht, The Netherlands, 2006; Part I, pp 627−631.
(23) Asano, A.; Takegoshi, K.; Hikichi, K. *Polymer* **1994**, *35*, 5630–5636 an intermediate domain size can be estimated from the spin diffusion rate: $^{1}/_{10}$ of the fastest T_1^H rate, in this case 1/1.06 s^{-1}, and the diffusion coefficient, 700 nm^2 s^{-1}. The diffusive path length in three dimensions, r, equals the root of (6 × 700/0.1), i.e., ca. 200 nm.
(24) Asano, A. *Kobunshi Ronbunshu*, **2007**, *64*, 406−418.
(25) Stejskal, E. O.; Schaefer, J.; Sefcik, M. D.; McKay, R. A. *Macromolecules* **1981**, *14*, 275–279.
(26) Asano, A.; Tanaka, C.; Kurotsu, T. *Macromolecules* **2008**, *41*, 9469–9473.
(27) Clauss, J.; Schmidt-Rohr, K.; Spiess, H. W. *Acta Polym*. **1993**, *44*, 1–17.
(28) Mellinger, F.; Wilhelm, M.; Spiess, H. W. *Macromolecules* **1999**, *32*, 4686–4691.
(29) Mirau, P. A. *A Practical Guide to Understanding the NMR of Polymers*; Wiley-Interscience: John Wiley & Sons, Inc.: Hoboken, NJ, 2005; Chapter 4, pp 248−335.
(30) Nishioka, M.; Takahashi, Y.; Kato, A.; Hikasa, S.; Iwabuki, H.; Nagata, K.; Asano, A. *Kobunshi Ronbunshu* **2009**, *66*, in press.
(31) Takahashi, Y.; Nishioka, M.; Kato, A.; Hikasa, S.; Iwabuki, H.; Nagata, K.; Asano, A. *Kobunshi Ronbunshu* **2009**, *66*, in press.
(32) Bucknall, C. B. In *Polymer Blends: Formulation and Performance*; Paul, D. R., Bucknall, C. B., Eds.; Wiley-Interscience: John Wiley & Sons, Inc.: New York, 2000; Vol. *2*, Chapters 21 and 22.
(33) Michler, G. H. *Acta Polym*. **1993**, *44*, 113–124.
(34) He, C.; Donald, A. M.; Butler, M. F. *Macromolecules* **1998**, *31*, 158–164.
(35) van der Sanden, M. C. M.; Buijs, L. G. C.; de Bie, F. O.; Meijer, H. E. H. *Polymer* **1994**, *35*, 2783–2792.
(36) Chen, H.; Yang, B.; Zhang, H. *J. Appl. Polym. Sci*. **2000**, *77*, 928–933.